J. Fluid Mech. (1981), *vol.* 111, *pp.* 347–366
Printed in Great Britain

The primary electroviscous effect in a suspension of rods

By J. D. SHERWOOD

Unilever Research, Port Sunlight Laboratory, Quarry Road East,
Bebington, Wirral, Merseyside

(Received 6 December 1980)

Calculations of the primary electroviscous effect have previously been restricted to spherical particles. Here we examine a suspension of randomly orientated rod-shaped particles of length l. Two competing mechanisms are present in a linear velocity field. The flow relative to each rod is largest at the rod ends. When l is large the consequent large distortion of the charge cloud increases the electroviscous effect. On the other hand, the given total charge on a uniformly charged rod is spread more thinly as l increases, and this tends to reduce the electroviscous effect. The balance of these two mechanisms is examined.

1. Introduction

Previous work on the primary electroviscous effect has concentrated on suspensions of uniformly charged spheres: see Booth (1950), Russel (1978), Lever (1979) and Sherwood (1980). Here we consider a suspension of rod-shaped particles of length l and radius a, where l is sufficiently small that the flow around each particle is governed by the Stokes equation. The motivation for this work is an experimental study of suspensions of the peptide polyglutamic acid by Domard (1976). Electroviscous effects were clearly important in his experiments and in certain cases we shall be able to explain his results.

Polyglutamic acid consists of a series of monomers each of which contains an ionizable group which either is, or is not, ionized. The molecule is therefore covered by a series of discrete charges rather than a continuous distribution of charge. In this paper both the non-spherical geometry and the non-uniform charge distribution will be examined. In §2 we shall consider a simple model of a polymer molecule with discrete charges placed along its length. The effect of the non-uniform charge distribution will be seen, as will that of the non-spherical geometry. In §3 we obtain asymptotic results for very long, uniformly charged rods by neglecting end effects. The polymers studied by Domard were not sufficiently long for this asymptotic theory to be valid. In §4 and §5 we therefore discuss a numerical study of a model which includes end effects. The theoretical predictions of this model are compared with Domard's experimental results.

The equilibrium charge cloud

We shall use as far as possible the notation of a previous paper (Sherwood 1980, henceforth denoted by I), and we recall some of the results obtained there. The charged polymer (or 'polyelectrolyte') is suspended in an electrolyte containing several species of ion, each with number density n^m and valence z^m, and with mobility ω (assumed

the same for all species – a reasonable assumption for ions of similar size). The total charge density ρ is

$$\rho = \sum_m n^m z^m e,$$

where e is the electronic charge. The electric potential ϕ is given by Poisson's equation:

$$\nabla^2\phi = -\rho/\epsilon.$$

Far from any charged particle the number densities of the ions attain limiting values n^m_∞, where

$$\sum_m n^m_\infty z^m e = 0$$

for electrical neutrality of the solution.

When the fluid velocity $\mathbf{u} = 0$ the charge cloud is in thermal equilibrium. Denoting equilibrium quantities by the subscript 0, the number density n^m_0 of the mth species of ion will be given by the Boltzmann distribution:

$$n^m_0 = n^m_\infty \exp(-ez^m\phi_0/kT).$$

Inserting this into Poisson's equation gives the Poisson–Boltzmann equation:

$$\nabla^2\phi_0 = -(e/\epsilon)\sum_m z^m n^m_\infty \exp(-ez^m\phi_0/kT).$$

When $e\phi_0 \ll kT$ this may be linearized to give

$$\nabla^2\phi_0 = \kappa^2\phi_0,$$

where

$$\kappa^2 = \frac{e^2}{\epsilon kT}\sum_m (z^m)^2 n^m_\infty.$$

The Debye length κ^{-1} is a typical size of the charge cloud. This linearized equation may be solved to give the potential around an infinite cylinder of radius a which carries a surface charge Q per unit length:

$$\phi_0 = \frac{\psi_0 K_0(\kappa r)}{K_0(\kappa a)} = \frac{Q}{2\pi\epsilon}\frac{K_0(\kappa r)}{a\kappa K_1(\kappa a)}, \tag{1}$$

where ψ_0 is the potential at the surface $r = a$, and K_0, K_1 are modified Bessel functions.

We may most easily study the non-linear Poisson–Boltzmann equation if we restrict ourselves to an electrolyte containing one species of positive monovalent ions and one of monovalent negative ions. Non-dimensionalizing the radial distance r from the origin by a, and setting $p = e\phi_0/kT$, the equation becomes

$$\frac{d^2p}{dr^2} + r^{-1}\frac{dp}{dr} = (a\kappa)^2 \sinh p,$$

where $p \to 0$ as $r \to \infty$ and the boundary condition at the surface of the cylinder is either $p = e\psi_0/kT$ or $p' = -Qe/2\pi a\epsilon kT$. This must be solved numerically. Far from the rod the potential is small and solutions take the form

$$p \sim Q^* K_0(a\kappa r)/a\kappa K_1(a\kappa)$$

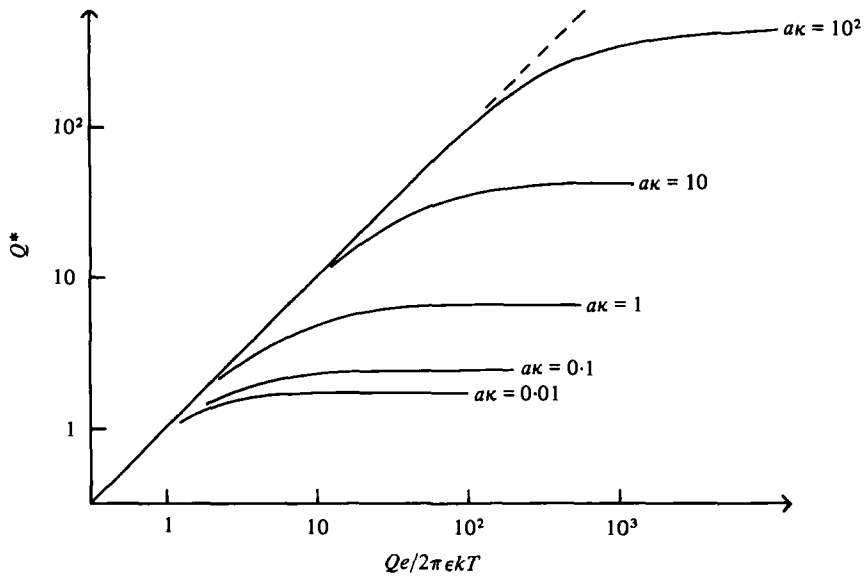

FIGURE 1. The coefficient of $K_0(a\kappa r)/a\kappa K_1(a\kappa)$ in the far field of the equilibrium cylindrical charge cloud around a rod of line charge density Q.

for some Q^*. When the line charge density Q is small the linearized solution is valid everywhere and

$$Q^* = Qe/2\pi\epsilon kT.$$

Numerical solutions of the Poisson–Boltzmann equation predict the far field behaviour shown in figure 1. At large charge densities Q^* approaches a limit $Q^*_{\text{lim}}(a\kappa)$ and the far field saturates. When $a\kappa \gg 1$ the charge cloud is thin and curvature may be neglected. From the analytic solution for a plane double layer we obtain

$$Q^*_{\text{lim}} \sim 4a\kappa \quad \text{as} \quad a\kappa \to \infty,$$

while Manning (1969) shows that

$$Q^*_{\text{lim}}(0) = (2\pi)^{-1}.$$

This corresponds to a line of isolated charges e separated by $7{\cdot}1 \times 10^{-10}$ m in water at 25 °C. In Domard's experiments $a\kappa$ is typically 10^{-2}, while the charge separation is $3{\cdot}6 \times 10^{-10}$ m, corresponding to $Q^* = 0{\cdot}3$. From figure 1 we see that saturation has not yet occurred. Saturation of the far field in spherical charge clouds was discussed in I. It was shown there that Booth's theory for the primary electroviscous effect at low potentials is in good agreement with full numerical calculations for thick charge clouds as long as saturation has not occurred. Henceforth we shall linearize the Poisson–Boltzmann equation, confident that the results will apply to Domard's experiments.

The distorted charge cloud

Suppose now that the fluid moves with velocity $\mathbf{u} = \mathbf{E}.\mathbf{r}$ relative to the centre of the rod, and that El is a typical value of $|\mathbf{u}|$. Then the Péclet number

$$P = El/\omega kT\kappa$$

measures the ratio of convection, which deforms the charge cloud away from equilibrium, to Brownian diffusion, which tries to restore equilibrium. We shall assume that the Péclet number is small, implying that the charge cloud is deformed only slightly. The potential ϕ and charge density ρ in the cloud may therefore be expanded as

$$\phi = \phi_0 + \phi_1 + \ldots, \quad \rho = \rho_0 + \rho_1 + \ldots,$$

where ϕ_1, ρ_1 are $O(P)$.

In I it was shown that the important non-equilibrium parameter is $\chi = \phi_1 + \rho_1/\kappa^2\epsilon$, which is obtained by solving

$$\left.\begin{aligned} \nabla^2\chi &= -\mathbf{u}.\nabla\rho_0/\omega kT\kappa^2\epsilon, \\ \chi &\to 0 \quad \text{at } \infty, \\ \mathbf{n}.\nabla\chi &= 0 \quad \text{on the surface of the particle.} \end{aligned}\right\} \tag{2}$$

$\nabla\chi$ is proportional to the non-equilibrium thermal and electrical forces acting on the charge cloud. These forces modify the flow around the suspended particle and the extent of this modification is measured by the Hartmann number:

$$H = \psi_0^2\epsilon/\mu_0\omega kT,$$

where μ_0 is the viscosity of the suspending fluid. H is the ratio of the electric forces in the charge cloud to the viscous forces.

When $H = 0$ the flow around the particle, held fixed in a straining flow $\mathbf{E}.\mathbf{x}$, is given by the Stokes equations and may be expressed in the form

$$u_i = F_{ijk}E_{jk}, \tag{3}$$

where $\mathbf{F}$ is a tensor which depends solely on the shape of the particle. In I it was shown that we may in general assume that the Hartmann number is small, and this we shall now do. We may therefore use the unperturbed velocity (3) when solving equation (2) for χ. If the particle number density n is sufficiently small that particle interactions may be neglected, the increase in stress in the suspension due to the primary electroviscous effect is

$$n\int_{V_f} \nabla\chi.\mathbf{F}\rho_0 dV, \tag{4}$$

where the integral is over V_f, the region outside a single charged particle.

Non-uniformly charged spherical particles

We have assumed that the ion Péclet number and Hartmann number are small, and that the electric potentials are sufficiently low that the Poisson–Boltzmann equation may be linearized. These are precisely the assumptions made by Booth (1950) in his study of uniformly charged spheres. He showed that the viscosity μ of a dilute suspension of spheres of radius a is

$$\mu = \mu_0\left(1 + \tfrac{5}{2}\Phi + \Phi\frac{\epsilon\psi_0^2(a\kappa)^2 f}{10\omega kT\mu_0}\right), \tag{5}$$

where Φ is the volume fraction of spheres, $\frac{5}{2}\Phi$ is Einstein's term, and f is a function of $a\kappa$ with asymptotes

$$\begin{aligned} f &\sim 150(a\kappa)^{-4} \quad (a\kappa \gg 1) \\ &\sim \tfrac{1}{2}(a\kappa)^{-3} \quad (a\kappa \ll 1). \end{aligned}$$

Note that the primary electroviscous effect is proportional to ψ_0^2. Non-uniformities in the surface charge will therefore be important. A simple example is that of a suspension of charged spherical particles each with surface potential $\psi_0 + \psi_1 \mathbf{D}.\mathbf{x}$. $\psi_1 \mathbf{D}.\mathbf{x}$ represents a dipole surface charge distribution. If ψ_1 is not small compared with ψ_0 the particles will tend to form chains, but ψ_1 and $\mathbf{D}$ are otherwise arbitrary. In the limit of a thin charge cloud ($a\kappa \gg 1$) the increase in stress in the suspension due to electric effects is

$$\frac{\epsilon\Phi}{\omega kT(a\kappa)^2}\{30\psi_0^2\mathbf{E} + \tfrac{40}{7}\psi_1^2\mathbf{E} + \tfrac{60}{14}\psi_1^2(\mathbf{E}.\mathbf{DD} + \mathbf{DE}.\mathbf{D})\}.$$

Assuming Brownian motion is sufficiently strong for $\mathbf{D}$ to be randomly oriented, this becomes

$$(30\psi_0^2 + 9\psi_1^2)\,\mathbf{E}\epsilon\Phi/\omega kT(a\kappa)^2.$$

This is very nearly proportional to the mean-squared surface potential $\overline{\psi^2} = \psi_0^2 + \frac{1}{3}\psi_1^2$, while electrophoresis measures the mean potential $\overline{\psi} = \psi_0$. Since $\overline{\psi^2} \geqslant (\overline{\psi})^2$ we conclude that, if we use the ζ-potential measured by electrophoresis, our predictions of the primary electroviscous effect will be too low unless the surface charge is uniform.

2. A simple model

We now study a simple model of a rod-shaped polymer molecule covered by a series of discrete charges. As the density of these charges increases we would expect the limit of a continuous distribution to be attained. Here we study the opposite limit: that in which the charges are so far apart that there are no interactions between their charge clouds. Note that electrical repulsion between the charges is now negligible. We must assume that the polymer's rigidity is structural rather than the result of electrical forces.

We model the polymer as a chain of charged beads linked by rigid rods. Such links are often considered to be hinged at the beads, but to model the rigid polymer molecule our links are required to lie in a line with direction $\mathbf{n}$. This is known as the 'shish-kebab model' (Riseman & Kirkwood 1950). The links have no effect on the flow, which can see only the beads and their surrounding charge clouds. The radius a of each bead is small compared with κ^{-1}, the size of its charge cloud. The major simplification of the model is that the separation of the charged beads is large compared with κ^{-1}.

The flow relative to the centre of the molecule is assumed linear: $\mathbf{u} = \mathbf{E}.\mathbf{x} + \boldsymbol{\Omega}.\mathbf{x}$, where $\mathbf{E}$ is the symmetric rate of strain and $\boldsymbol{\Omega}$ the vorticity. However, the vorticity merely rotates the rods and, as explained by Russel (1978), this motion may be ignored. There are N beads evenly spaced along the rod of length l. Each bead has charge Q and hence the total charge on the molecule is $Q_T = NQ$. For definiteness we choose N odd, so that the beads are positioned at the points $s_i\mathbf{n}$, where s_i, the distance of the ith bead from the centre of the rod, has the values

$$s_i = il/N \quad (i = (-\tfrac{1}{2}(N-1), \ldots, -1, 0, 1, \ldots, \tfrac{1}{2}(N-1))).$$

The case $N = 5$ is illustrated in figure 3. The flow in the neighbourhood of the ith bead consists of a uniform flow $\mathbf{U} = \mathbf{E}.s_i\mathbf{n}$ superposed on the linear straining $\mathbf{E}.(\mathbf{x} - s_i\mathbf{n})$.

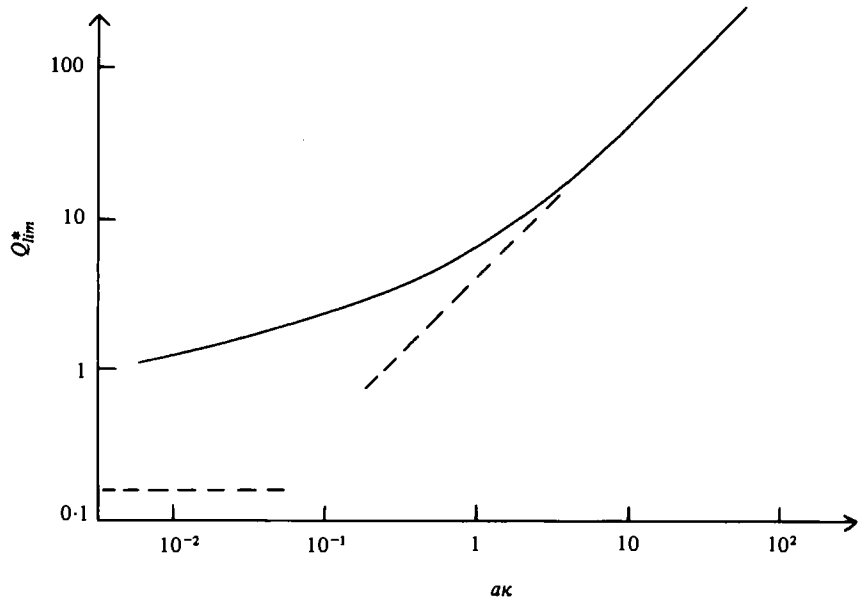

FIGURE 2. $Q^*_{\lim}$ = coefficient of $K_0(a\kappa r)/a\kappa K_1(a\kappa)$ in a saturated equilibrium charge cloud, as a function of $a\kappa$. The asymptotes as $a\kappa \to \infty$ and $a\kappa = 0$ are shown as broken lines.

These two velocities contribute separately to the stress, and we deal first with the straining part of the flow. The contribution of this to the stress is well known. Each bead introduces an additional stress $20\pi a^3\mu_0 \mathbf{E}/3$ (Einstein 1911), whilst each charge cloud contributes $\mathbf{E}Q^2/120\pi\omega kT\epsilon\kappa$ (Booth 1950; our equation (5)). (Note that this result is more naturally expressed in terms of Q rather than ψ_0. The exact size of the particle is not important in the limit of thick charge clouds $a\kappa \ll 1$.) Summation over the N beads gives an increase in the stress of

$$N\left\{\tfrac{20}{3}\pi a^3\mu_0 + \frac{Q^2}{120\pi\omega kT\epsilon\kappa}\right\}\mathbf{E}. \tag{6}$$

We now consider the uniform flow $\mathbf{U}$ past each bead. This induces a drag which consists of the Stokes drag $6\pi a\mu_0\mathbf{U}$ together with the drag on the cloud, found by Booth (1954) to be $\kappa Q^2\mathbf{U}/24\pi\omega kT\epsilon$ in the limit of a thick cloud. If the force on the ith bead is $\mathbf{F}_i$, then these forces contribute $\sum_i s_i \mathbf{n}\mathbf{F}_i$ to the stress. If no Brownian motion is present the rod rotates with the transverse flow and

$$\dot{\mathbf{n}} = \mathbf{E}.\mathbf{n} - \mathbf{n}\mathbf{n}.\mathbf{E}.\mathbf{n} + \boldsymbol{\Omega}.\mathbf{n}.$$

In steady state the probability distribution function $p(\mathbf{n})$ satisfies the diffusion equation

$$\nabla.(p\dot{\mathbf{n}} - D\nabla p) = 0,$$

where D is the rotary diffusion coefficient. We shall assume that rotary Brownian motion is strong. The diffusion equation has solution

$$p(\mathbf{n}) = \frac{1}{4\pi} + \frac{\mathbf{n}.\mathbf{E}.\mathbf{n}}{8\pi D} + O\left(\frac{|\mathbf{E}|}{D}\right)^2.$$

The random orientation of the rods is only slightly perturbed, and the rotation caused by Brownian couples is equal and opposite to that caused by the straining flow $\mathbf{E}.\mathbf{x}$. The sum of the Brownian and hydrodynamic contributions to the stress becomes

$$\sum_i s_i \mathbf{n}\mathbf{F}_i = \sum_i s_i \mathbf{n} F \mathbf{E}.\mathbf{n}\mathbf{s}_i = F\mathbf{n}.\mathbf{E}.\mathbf{n}(N-1)(N+1)l^2/12N,$$

where

$$F = 6\pi a\mu_0 + \kappa Q^2/24\pi\omega kT\epsilon.$$

Averaging over the random orientation gives the stress

$$F(N-1)(N+1)l^2\mathbf{E}/36N. \tag{7}$$

The sum of (6) and (7) gives the total contribution to the stress, per particle. As $a \to 0$ the electrical terms dominate and the stress in the suspension becomes

$$\boldsymbol{\sigma}^E = \frac{nQ_T^2\mathbf{E}}{\omega kT\kappa\epsilon}\left\{\frac{1}{120\pi N} + \frac{(N-1)(N+1)l^2\kappa^2}{864\pi N^3}\right\},$$

where n is the number density of rods in the suspension. We see at once that $|\boldsymbol{\sigma}^E| \sim (l\kappa)^2$ as $l \to \infty$. The ends of the rod are brought into regions of ever increasing flow strength. The correspondingly large distortions of the charge cloud produce a large electroviscous effect. On the other hand,

$$\boldsymbol{\sigma}^E \to \frac{Q_T^2 n\mathbf{E}}{120\pi N\omega kT\kappa\epsilon} \quad \text{as} \quad l \to 0.$$

This is smaller than the corresponding result for a charged sphere by a factor N^{-1}. The model has ignored interactions between the charge clouds which have now coalesced. Similarly, if we make our rod uniformly charged by letting $N \to \infty$, we find that $|\boldsymbol{\sigma}^E| \sim N^{-1}$, which is clearly incorrect. The interactions between overlapping charge clouds have again been ignored.

Finally, let us consider electrophoresis of our charged particle in an electric field $\mathbf{E}$. If the charge on the ith bead is Q_i, the velocity of the particle is

$$\mathbf{U} = \mathbf{E}\sum_{i=1}^{N} Q_i/6\pi a\mu_0 N$$

(since the charge clouds are thick compared with the size of the beads). Suppose $Q_i = \pm Q$. $\mathbf{U}$ is proportional to the total charge on the particle and is zero at the isoelectric point. However, the electroviscous effect is unchanged and proportional to Q^2.

3. Very long rods

In the previous section we assumed no interaction between the charge clouds, but this is unrealistic in typical experimental conditions. We now perform an analysis valid for very long, uniformly charged, rods. Each rod is taken to be a cylinder of length l, radius a, with $l \gg a$, and we take the Debye length $\kappa^{-1} \ll l$ so that end effects may be neglected. This implies that the unperturbed charge cloud is independent of position along the rod, and so velocities along the rod produce no distortion of the cloud (except at the ends, which we ignore). It also implies that, close to the surface,

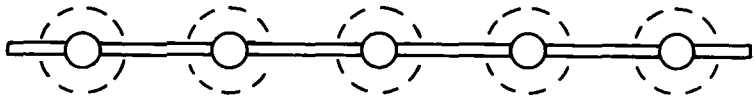

FIGURE 3. The shish-kebab model when $N = 5$.

derivatives of $\mathbf{u}$ and χ along the rod are negligible compared with those perpendicular to its axis. The problem is two-dimensional, and the equilibrium potential in the cloud is given by (1). We assume that the flow is weak compared with Brownian rotation of the particle: i.e. $\gamma/D \ll 1$, where γ = rate of shear, $D = kT/R_w$, and R_w is the resistance coefficient for rotation, i.e.

$$\frac{\gamma}{kT}\frac{\pi\mu_0 l^3}{3\{\log(l/a)-\frac{1}{2}\}} \ll 1. \tag{8}$$

Rotation by the symmetric extensional flow $\mathbf{E}$ will be balanced by Brownian couples, which orientate the rods randomly. As in § 2, we may take the rods to be stationary with respect to $\mathbf{E}$ and may neglect the effects of vorticity. Strong Brownian motion of the particles implies that Brownian diffusion of the very much smaller ions is strong, i.e. that the ion-Péclet number $\gamma l/\omega kT\kappa \ll 1$, which is clear from (8) when we note that ω is typically 4×10^{11} m/N s.

We now choose cartesian axes (x_1, x_2, x_3) such that x_1 is measured along the rod. We may orientate the 2, 3 axes so that on $x_2 = x_3 = 0$ the unperturbed flow perpendicular to the rod would be $E_{21}x_1$. To solve our governing equation (2) for χ, the distortion of the charge cloud, we must know $\mathbf{u}.\nabla\rho_0$, and since $\kappa^{-1} \ll l$ we are interested in $\mathbf{u}$ only close to the rod. We therefore use the inner expansion of a pair of matched asymptotic expansions, as given by Cox (1970). In cylindrical co-ordinates the inner expansion is

$$\begin{aligned}
u_r &= c\cos\theta\,(1-a^2/r^2-2\ln r/a)/\ln(a/l)+O(\ln a/l)^{-2},\\
u_\theta &= c\sin\theta\,(1-a^2/r^2+2\ln r/a)/\ln(a/l)+O(\ln a/l)^{-2},\\
u_1 &= d\ln(r/a)/\ln(a/l) \qquad\qquad +O(\ln a/l)^{-2},
\end{aligned}$$

where the constants c, d are to be found by matching with the outer velocity $\mathbf{u} = \mathbf{E}.\mathbf{x}$, giving

$$c = \tfrac{1}{2}E_{21}x_1 = \tfrac{1}{4}(E_{21}+E_{12})\,x_1, \quad d = -E_{11}x_1,$$

where we have symmetrized c and d, since this is the form required for evaluation of the tensor $\mathbf{F}$.

Neglecting the non-uniformity of the equilibrium charge cloud at the ends, only the radial component of velocity contributes to $\mathbf{u}.\nabla\rho_0$ and the equation for χ becomes

$$\nabla^2\chi = \frac{-c\psi_0\epsilon\kappa^2\cos\theta}{\ln(a/l)\,K_0(a\kappa)\,\omega kT\kappa^2\epsilon}\,(1-a^2/r^2-2\ln r/a)\frac{\partial K_0(\kappa r)}{\partial r}.$$

Setting $z = r/a$, this has solution $\chi = A\chi_1\cos\theta$, where

$$A = -c\psi_0 a^2\kappa/\ln(a/l)\,\omega kT K_0(a\kappa),$$

$$\chi_1(z) = -\tfrac{1}{2}\left\{(z+z^{-1})\int_1^\infty X(\xi)\,d\xi + z^{-1}\int_1^z X(\xi)\xi^2\,d\xi - z\int_1^z X(\xi)\,d\xi\right\}$$

and

$$X(z) = (1-z^{-2}-2\ln z)\,K_0'(a\kappa z).$$

We now evaluate the increase in stress (4). Again neglecting end effects the (2, 1) and (1, 2) components of $F_{kij}\partial\rho_0/\partial x_k$ are

$$-(1-a^2/r^2-2\ln r/a)\,x_1\cos\theta\psi_0\epsilon\kappa^3K_0'(\kappa r)/4\,(\ln a/l)\,K_0(a\kappa)$$

and all other components are smaller by a factor $(\ln a/l)^{-1}$. Integrating over all space outside the rod, the increase in stress due to the charge cloud around one rod is

$$-\{(\mathbf{E}.\mathbf{n}-\mathbf{nn}.\mathbf{E}.\mathbf{n})\,\mathbf{n}+\mathbf{n}(\mathbf{E}.\mathbf{n}-\mathbf{nn}.\mathbf{E}.\mathbf{n})\}\frac{l^3\psi_0^2\epsilon(a\kappa)^5\pi F(a\kappa)}{96\omega kT\,(\ln a/l)^2K_0^2(a\kappa)},$$

where

$$F(a\kappa)=-\int_1^\infty K_1(a\kappa z)\,z(1-z^{-2}-2\ln z)\,\chi_1(z)\,(a\kappa)^{-1}\,dz,$$

which may be put in the form

$$\begin{aligned}F(a\kappa)=(a\kappa)^{-3}&\int_1^\infty 2K_0(a\kappa z)\,(z^{-3}-z^{-1})\,dz\int_1^\infty K_0(a\kappa z)\,(z^{-1}-z^{-3}+2z\ln z)\,dz\\&+(a\kappa)^{-3}\int_1^\infty K_0^2(a\kappa z)\,\{-4z(\ln z)^2+4z\ln z-4z^{-1}\ln z-z+2z^{-1}-z^{-3}\}\,dz\\&-4(a\kappa)^{-5}\int_1^\infty K_0(a\kappa)\,K_0(a\kappa z)\,(z^{-1}-z^{-3})\,dz\\&+(a\kappa)^{-5}\int_1^\infty K_0^2(a\kappa z)\,(12z^{-1}-12z^{-3}+8z^{-3}\ln z)\,dz.\end{aligned}$$

The asymptotic expansions are

$$\begin{aligned}F(a\kappa)&\sim(a\kappa)^{-5}\{-2(\ln a\kappa)^2-2{\cdot}2464\ln a\kappa-3{\cdot}1726\}+\ldots\quad\text{as}\quad a\kappa\to0\\&\sim-8\pi e^{-2a\kappa}(a\kappa)^{-8}+81{\cdot}5\pi e^{-2a\kappa}(a\kappa)^{-9}+\ldots\quad\text{as}\quad a\kappa\to\infty,\end{aligned}$$

with 95 % accuracy at 0·01 and 50 respectively. Typical values of $F(a\kappa)$, for the range of $a\kappa$ used in the experiments discussed in §5.5, are

$a\kappa$	$F(a\kappa)$	$F(a\kappa)\,(a\kappa)^5/K_0^2(a\kappa)$
$10{\cdot}87\times10^{-2}$	$-0{\cdot}4287\times10^6$	1·183
$3{\cdot}87\times10^{-2}$	$-0{\cdot}1770\times10^9$	1·354

We now use our assumption that Brownian motion is strong, and average over the uniformly distributed orientations of $\mathbf{n}$. The increase in viscosity due to electrical effects, μ_{NS}, in a suspension of volume fraction Φ is

$$\mu_{\mathrm{NS}}=\frac{-\Phi(l/a)^2\psi_0^2\epsilon(a\kappa)^5F(a\kappa)}{480\omega kT(\ln a/l)^2K_0^2(a\kappa)}. \tag{9}$$

The total charge on each rod is

$$Q_T=2\pi a\kappa l\psi_0\epsilon K_1(a\kappa)/K_0(a\kappa).$$

In terms of Q_T, we obtain

$$\mu_{\mathrm{NS}}\sim\Phi Q_T^2(\log a\kappa)^2/960\pi^2a^2\omega kT\epsilon(\ln a/l)^2\quad\text{as}\quad a\kappa\to0. \tag{10}$$

We shall discuss in §5.4 the lack of agreement between this prediction and the experimental results of Domard. In the next section we discuss a full numerical solution of the governing equations. We shall find that (9) and (10) are valid only when $l>20\kappa^{-1}$.

If the rod is uniformly charged but free-draining (in the sense that it has no effect on the imposed flow except via its charge cloud – cf. the discrete charge model of §2) then similar calculations give the increase in the viscosity of the suspension:

$$\mu_{\mathrm{FD}} = \Phi\psi_0^2\epsilon(l\kappa)^2\{K_0^2(a\kappa)+K_1^2(a\kappa)\}/240\omega kTK_1^2(a\kappa)$$
$$\sim \mu_{\mathrm{NS}}(\log a/l)^2/(\log a\kappa)^2 \quad \text{as} \quad a\kappa\to 0. \tag{11}$$

The unperturbed flow has not been slowed down by the presence of the rod, and the large distortion of the charge cloud gives rise to a large electroviscous effect. This result will be used as a check on the numerical scheme discussed below.

4. A full numerical scheme

The results of §3 are not suitable for comparison with Domard's experiments for two reasons. Electroviscous effects are largest and most easily measured when the charge cloud is thick. We therefore wish to remove the constraint $\kappa^{-1} \ll l$ by improving the representation of the charge cloud to include end effects. Secondly, Cox's (1970) inner expansion of the velocity field is correct only to $O(\log l/a)^{-1}$. Even when $l/a = 45$, $\log(l/a)$ is only 3·8, so we wish also to improve the representation of the velocity field. We now set up a full numerical scheme which incorporates both these improvements.

The fluid velocity may be expressed as a distribution of Stokeslets over the surface of the particle. When the body is slender, as in this case, we may approximate this distribution by one of Stokeslets and multipoles along the centre-line. Here we follow Lighthill (1976) and consider Stokeslets and source dipoles, since the strength of the latter is determined by the local Stokeslet strength. We seek to satisfy as nearly as possible the no-slip condition on the surface of the particle. Lighthill discusses how the rod may be divided into M discrete elements over each of which the Stokeslet strength is constant. Accuracies $O(a/l)$ can be attained. This may be used as the basis of a numerical method which is described by Russel *et al.* (1977) and by Higdon (1979). We omit the details, and merely observe that the flow due to the Stokeslets, together with the imposed flow $\mathbf{E}.\mathbf{x}$, may be expressed in the form

$$\left.\begin{aligned}\mathbf{u} = \hat{\mathbf{x}}_1\{&E_{11}(C+x_1)+\tfrac{1}{2}(E_{12}+E_{21})(A+r)\cos\theta\}+\hat{\mathbf{r}}\{E_{11}(D-\tfrac{1}{2}r)\\&+\tfrac{1}{2}(E_{12}+E_{21})(B+x_1)\cos\theta+\tfrac{1}{2}(E_{22}-E_{33})r\cos 2\theta+\tfrac{1}{2}(E_{23}+E_{32})r\sin 2\theta\}\\&+\hat{\boldsymbol{\theta}}u_\theta,\end{aligned}\right\} \tag{12}$$

where $\hat{\mathbf{x}}_1$, $\hat{\mathbf{r}}$, $\hat{\boldsymbol{\theta}}$ are unit vectors, with $\hat{\mathbf{x}}_1$ along the rod, and A, B, C, D are functions of position which represent the flow due to the Stokeslets.

We assume that the charge along the rod consists of a series of discrete charges Q at points $\mathbf{r}_i$ $(i = 1, \ldots, N)$. The charge cloud is given by superposition:

$$\rho_0(\mathbf{r}) = -\sum_{i=1}^{N} Q\kappa^2\exp[-\kappa|\mathbf{r}-\mathbf{r}_i|/4\pi|\mathbf{r}-\mathbf{r}_i|]$$

and, as in §2, we shall distribute the charges uniformly along the rod, at points

$$\mathbf{r}_i = (r, x_i) = (0, il/N); \quad i = -\tfrac{1}{2}(N-1), \ldots, -1, 0, 1, \ldots, \tfrac{1}{2}(N+1).$$

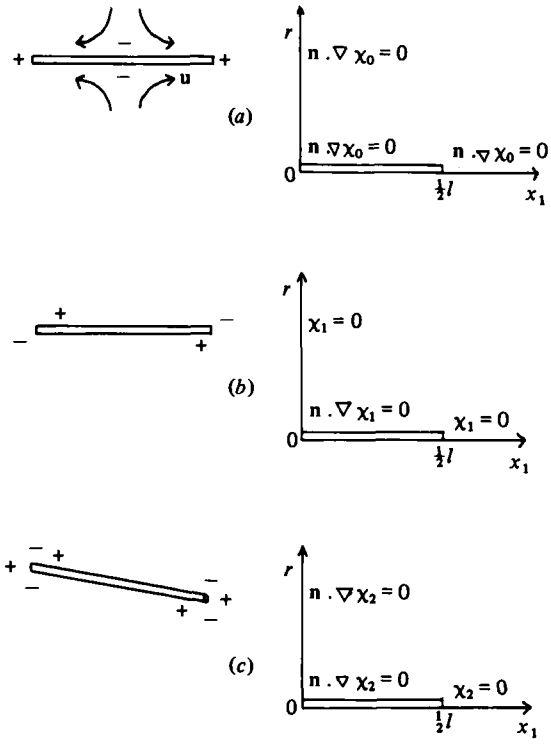

FIGURE 4. The boundary conditions for (*a*) χ_0, (*b*) χ_1, (*c*) χ_2, together with the corresponding distortions of the charge cloud.

As discussed above, this discrete representation of charge is realistic, and in the limit $N \to \infty$ we recover a uniformly charged rod.

We must now obtain χ by solving equation (2). $\nabla\rho_0$ is independent of θ, so we may make a Fourier decomposition of χ similar to that of $\mathbf{u}$:

$$\chi = \{\chi_0 E_{11} + \tfrac{1}{2}\chi_1 \cos\theta(E_{12}+E_{21}) + \tfrac{1}{2}\chi_2[(E_{22}-E_{33})\cos 2\theta + (E_{23}+E_{32})\sin 2\theta]\}/\omega kT\kappa^2\epsilon.$$

χ_0 satisfies the equation

$$\frac{\partial^2\chi_0}{\partial r^2} + r^{-1}\frac{\partial\chi_0}{\partial r} + \frac{\partial^2\chi_0}{\partial x_1^2} = (C+x_1)\frac{\partial\rho_0}{\partial x_1} + (D-\tfrac{1}{2}r)\frac{\partial\rho_0}{\partial r}.$$

In the far field χ_0 is a quadrupole of the form $P_2^0(\cos\phi)\, r_s^{-3}$ where ϕ is measured from the x_1-axis, and $r_s^2 = r^2 + x_1^2$. Thus $\chi_0 \propto (2x_1^2 - r^2) r_s^{-5}$ at infinity. The boundary conditions are illustrated in figure 4, together with the corresponding distortion of the charge cloud.

χ_1 satisfies

$$\frac{\partial^2\chi_1}{\partial r^2} + r^{-1}\frac{\partial\chi_1}{\partial r} - \frac{\chi_1}{r^2} + \frac{\partial^2\chi_1}{\partial x_1^2} = (A+r)\frac{\partial\rho_0}{\partial x_1} + (B+x_1)\frac{\partial\rho_0}{\partial r}.$$

χ_1 is analogous to the χ_1 of § 3. The far field is a quadrupole of the form $\cos\theta\, P_2^1(\cos\phi)\, r_s^{-3}$ which implies $\chi_1 \propto r x_1 r_s^{-5}$ at infinity. Similarly

$$\frac{\partial^2\chi_2}{\partial r^2} + r^{-1}\frac{\partial\chi_2}{\partial r} - 4r^{-2}\chi_2 + \frac{\partial^2\chi_2}{\partial x_1^2} = r\frac{\partial\rho_0}{\partial r}.$$

The far field is of the form $\sin 2\theta P_2^2(\cos\phi)\, r_s^{-3}$ so $\chi_2 \propto r^2 r_s^{-5}$ at infinity.

The increase in the stress is given by our standard integral (4). From (12) we see that the relevant components of $\mathbf{F}$ are

$$F_{r11} = D - \tfrac{1}{2}r, \qquad F_{r23} = F_{r32} = \tfrac{1}{2}r\sin 2\theta,$$
$$F_{r12} = F_{r21} = \tfrac{1}{2}(B + x_1)\cos\theta, \qquad F_{x11} = C + x_1,$$
$$F_{r22} = -F_{r33} = \tfrac{1}{2}r\cos 2\theta, \qquad F_{x12} = F_{x21} = \tfrac{1}{2}(A + r)\cos\theta.$$

Integration with respect to θ eliminates many of the terms of (4), of which the non-zero components are

$$(1,1)\text{ component} = -\int_{V_f}\left[\frac{\partial\rho}{\partial r}(D - \tfrac{1}{2}r) + \frac{\partial\rho}{\partial x_1}(C + x_1)\right]\chi_0 E_{11}\, dV/\omega kT\kappa^2\epsilon = G_1 E_{11}, \quad \text{say},$$

$$(1,2) = (2,1) = -\int_{V_f}\left[\frac{\partial\rho}{\partial r}(B + x_1) + \frac{\partial\rho}{\partial x_1}(A + r)\right]\chi_1\cos^2\theta(E_{12} + E_{21})\, dV/4\omega kT\kappa^2\epsilon$$
$$= \tfrac{1}{2}G_2(E_{12} + E_{21}),$$

$$(2,2) = -(3,3) = -\int_{V_f}\frac{\partial\rho}{\partial r} r\cos^2 2\theta\chi_2(E_{22} - E_{33})\, dV/4\omega kT\kappa^2\epsilon = \tfrac{1}{2}G_3(E_{22} - E_{33}),$$

$$(2,3) = (3,2) = \tfrac{1}{2}G_3(E_{23} + E_{32}).$$

Adding an isotropic stress $\frac{1}{2}G_3(E_{22} + E_{33})\,\mathbf{I}$, the electrical contribution to the stress may be written as

$$\boldsymbol{\sigma}_{\text{elec}} = G_3\mathbf{E} + (G_2 - G_3)(\mathbf{E}.\mathbf{nn} + \mathbf{nE}.\mathbf{n}) + (G_1 - 2G_2 + \tfrac{1}{2}G_3)\,\mathbf{nnn}.\mathbf{E}.\mathbf{n}.$$

Averaging over all orientations $\mathbf{n}$ with equal probability, since Brownian motion is strong, we obtain

$$\boldsymbol{\sigma}_{\text{elec}} = (\tfrac{2}{15}G_1 + \tfrac{2}{5}G_2 + \tfrac{2}{5}G_3)\mathbf{E}.$$

5. Numerical methods and results

The velocity field

The first step of the calculation is to find the Stokeslet strengths. Our goal is to explain the intrinsic viscosity of a suspension of charged rods. Domard measured an intrinsic viscosity $[\eta]$, which he defined as

$$[\eta] = \lim_{\Phi\to 0}\frac{\mu - \mu_0}{\mu_0\Phi}\frac{V}{m_T}, \tag{13}$$

where V, m_T are the volume and mass of one particle. We shall assume that the density m_T/V is not far from that of water. The electroviscous contribution will be evaluated later, but first we must find the intrinsic viscosity due to uncharged rods. We require the couple L_2 on a rod rotating about an axis perpendicular to itself, and the stresslet S_{11} when the rod is placed in a pure axially symmetric straining motion.

The general behaviour of the numerical results has been discussed by Russel *et al.* (1977). Convergence of the iterative scheme is rapid as long as the centres of all elements are further than a radius from the ends of the rod. This puts an upper bound on the number of elements M into which the rod may be divided. For sufficiently large M the results are independent of M, but for short rods this limit cannot be attained. It is therefore necessary to extrapolate the results out to $M = \infty$. The com-

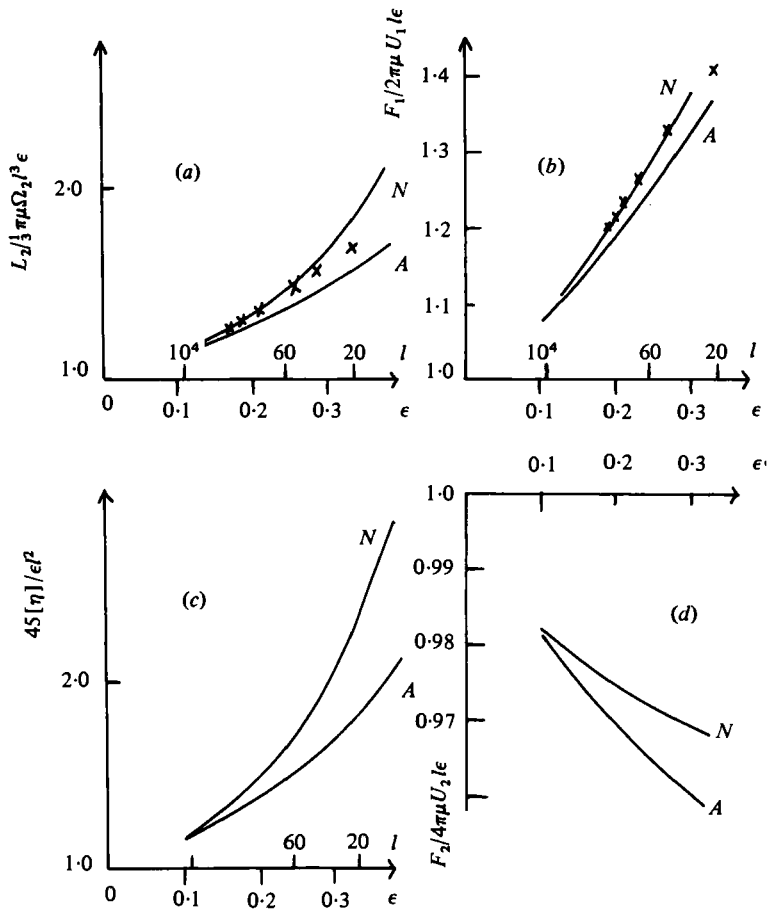

FIGURE 5. Results for the friction coefficients for a rod of length l and radius a. (*a*) L_2 for rotation about an axis perpendicular to the centre-line, (*b*) F_1 for translation along the axis, (*c*) intrinsic viscosity, and (*d*) F_2 for translation perpendicular to the axis, all scaled by first-order slender body theory. N indicates numerical results; A, Batchelor's (1970) 3rd-order asymptotic theory; and X, Youngren & Acrivos' (1975) numerical results. $\epsilon = 1/\log(l/a)$.

putations performed here suggest that the numerical error as $M \to \infty$ varies more closely with M^{-1} than with the $M^{-1}\log M$ found by Russel *et al.* These authors give results for aspect ratios $l/2a \geqslant 20$ in their figure 3, after extrapolation to $M = \infty$ and normalization by the asymptotic predictions of first-order slender-body theory. For comparison they also plot Batchelor's (1970) third-order approximation, and the exact numerical calculations of Youngren & Acrivos (1975). We are interested in aspect ratios as low as 9, so we present our own calculations in the same manner in figure 5. Note that Russel *et al.* plot Youngren & Acrivos' results for L_2 incorrectly and that the discrepancy between the two sets of numerical results appears incorrectly to grow at large aspect ratios. From our figure 5 we see that the discrepancy is only 4% at an aspect ratio 25, and agreement is excellent at higher aspect ratios. We plot the intrinsic viscosity rather than S_{11}, since Youngren & Acrivos did not compute any values for S_{11}. For completeness we also show the friction coefficients F_1 and F_2 for translation of a rod along and perpendicular to its axis. The assumption

Aspect ratio $l/2a$	$[\eta]$ experimental (charged rods)	$[\eta]$ 3rd-order approximation	$[\eta]$ numerical results
9	26	9·4	12
12·15	46	14·4	17
17·1	72	24·1	29
22·5	130	37·2	43
180	800 or less	1286·6	

TABLE 1. Values of the intrinsic viscosity of a suspension of rods

that as $M \to \infty$ the error term varies as M^{-1} (rather than $M^{-1}\log M$) improves the agreement between the slender-body results for F_1 and Youngren & Acrivos' results, whilst for F_2 it removes the peculiar turning point found by Russel *et al.*

In table 1 we compare these numerical results for $[\eta]$ with Batchelor's third-order theory and with Domard's experimental measurements. We see from the experiments that electrical effects have approximately doubled the intrinsic viscosity of the suspension. Having obtained the Stokeslet distribution, the number of elements M did not greatly affect the further calculations of the electroviscous effect. M was therefore taken to be 31, or, in the case of short rods, the largest value which still gave convergence.

The electroviscous effect

We are now in a position to find χ by solving the three problems depicted in figure 4. We simplify the problem by assuming that $a \ll \kappa^{-1}$ (as was the case in Domard's experiments). With errors $O(a\kappa)^2$ we may apply the boundary conditions

$$\partial\chi_0/\partial r = 0 \quad (\chi_1 = \chi_2 = 0)$$

on the axis of the rod, rather than the appropriate condition at its surface. By evaluating the quadrupole moment of χ we obtain boundary values for χ far from the rod, where higher multipoles may be neglected. The final solution was found not to depend very strongly on the position of the outer boundary, which was usually taken to be along the lines

$$r = x_1 = 2l + 10\kappa^{-1}.$$

Thus for a point charge the integration extended to 10 Debye lengths, whilst for a long rod the $O(r_s^{-5})$ term which was neglected at the outer boundary was about 6% of the $O(r_s^{-3})$ quadrupole term.

Because the rod has been approximated by a line, the ratio κ^{-1}/a must always be large but is no longer physically important. On the other hand, the ratio κ^{-1}/l is quite crucial. Setting $a = 1, \kappa^{-1}$ was chosen to be 10 and the entire range of values for l was investigated. Each of the problems depicted in figure 4 was then solved using successive over-relaxation over a rectangular grid. A uniform grid mesh was ideal for studying the experimental results, and was used throughout, though a variable mesh-size might have improved efficiency for extremely large values of l. Variation of the position of the boundaries and of the grid size produced answers which varied by some 15%, and this is therefore the suggested accuracy of the results presented here. All results are non-dimensionalized by the electroviscous effect which would be

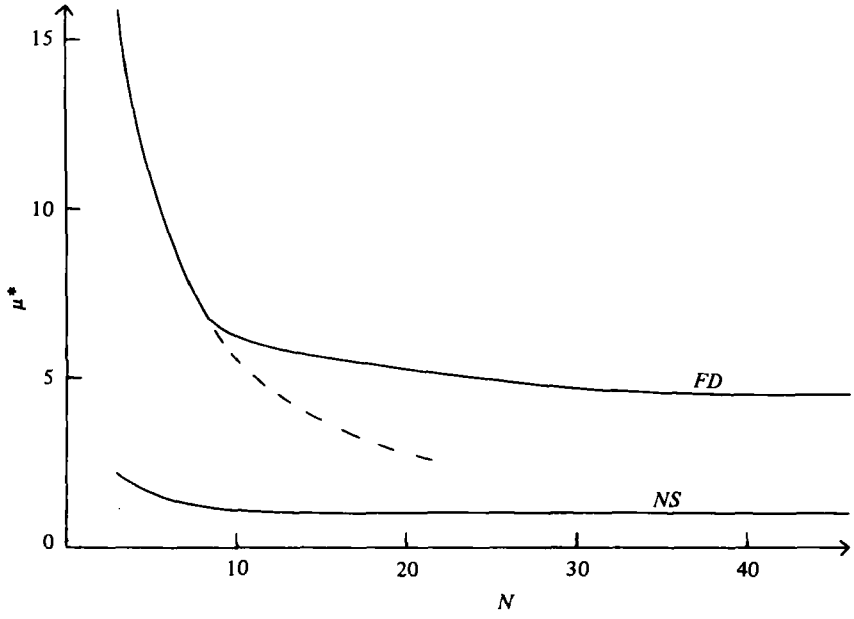

FIGURE 6. Non-dimensional intrinsic viscosity μ^*. FD, free-draining rods; NS, rods with no-slip boundary condition, as a function of the number of charges N. The broken line shows the asymptotic result (14). $l = 200$, $\kappa^{-1} = 10$.

present if the charges were concentrated at a point instead of spaced along a line. From (5) we see that this value is

$$Q_T^2 n/240\pi\omega kT\kappa\epsilon,$$

where n is the number density of particles in the suspension.

Free-draining rods

The program was first tested by evaluating the electroviscous effect in a suspension of point charges. This has magnitude 1 under the present normalization. The scheme for finding the Stokeslet strengths naturally did not converge, as it was designed for slender rods, but since a point charge does not affect the flow in the bulk of the charge cloud (Lever 1979) the Stokeslet strengths were simply set to zero. The computed result was accurate to within 4 %.

After normalization the viscosity of a suspension of free-draining rods, discussed in § 2, becomes

$$\mu^*_{\mathrm{FD}} = N^{-1} + 5(N-1)(N+1)l^2\kappa^2/36N^3. \tag{14}$$

This result is exact as long as the point charges are sufficiently separated for their charge clouds not to interact. We may study these interactions by setting the Stokeslet strengths to zero in this full numerical scheme, so that the rod becomes free-draining. Figure 6 shows the numerical results obtained for a free-draining rod of length $l = 200$ as the number of charges N is increased. The analytic prediction (14) is shown as a broken line. Agreement is good when $N \leqslant 10$, i.e. when the distance between charges is greater than $2\kappa^{-1}$. When N becomes large the theory for a long, uniformly charged free-draining rod becomes valid (see (11)) predicting $\mu^*_{\mathrm{FD}} = 5$. The numerical result is 4·5 and the difference reflects the presence of end-effects.

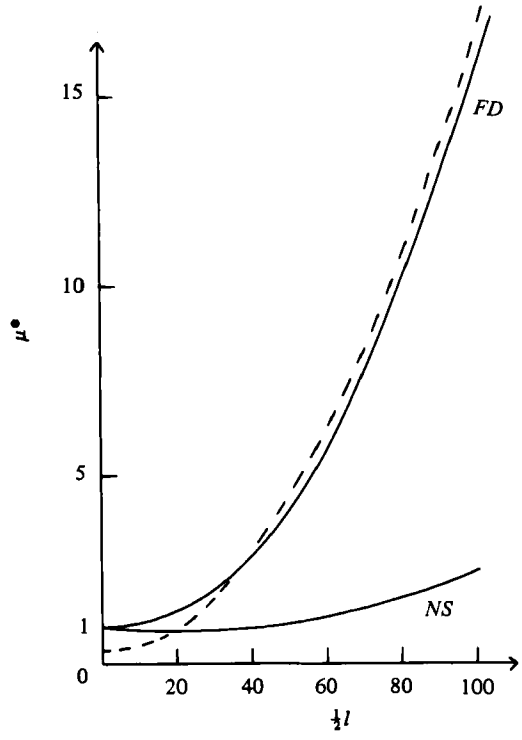

FIGURE 7. Non-dimensional intrinsic viscosity μ^*. NS, rods with no-slip boundary condition; FD, free-draining rods, as a function of the half-length $\frac{1}{2}l$. The broken line shows the asymptotic result (14). Number of charges $N = 3$.

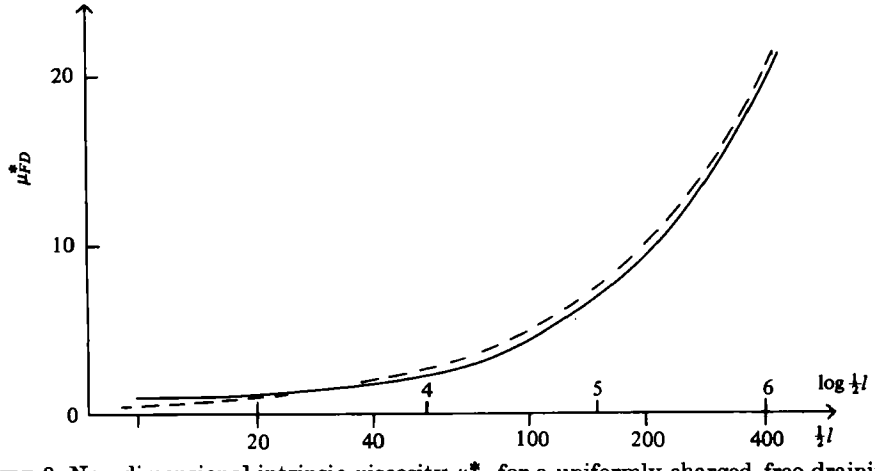

FIGURE 8. Non-dimensional intrinsic viscosity μ^*_{FD} for a uniformly charged free-draining rod as a function of the half-length $\frac{1}{2}l$. The broken line shows the asymptotic result (11).

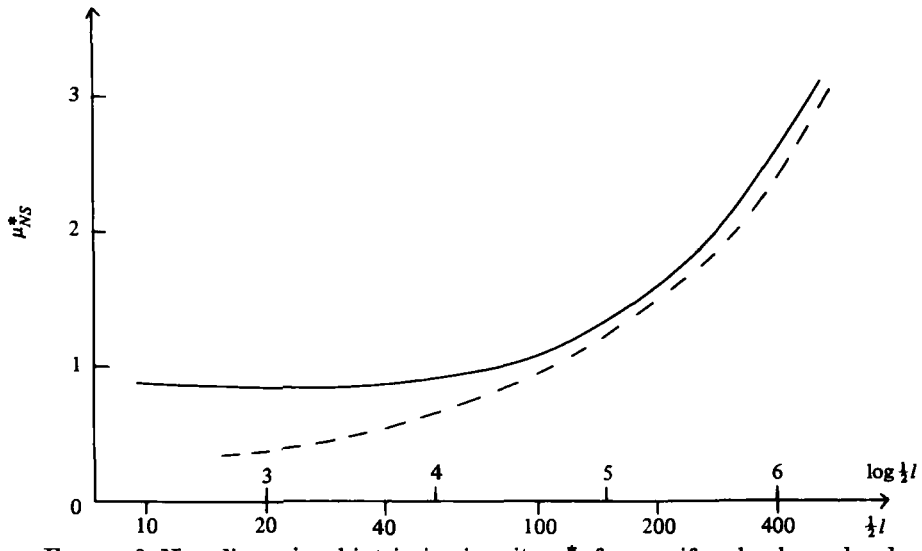

FIGURE 9. Non-dimensional intrinsic viscosity μ^*_{NS} for a uniformly charged rod with no-slip boundary conditions. The broken line shows the asymptotic result (15).

In figure 7 we fix the number of charges at 3 and vary the rod length l. The percentage difference between the numerical results and the prediction (14) is 11 % at $l = 100$, again indicating the accuracy of the numerical scheme. In figure 8 the density of charges is sufficiently high that the rod may be regarded as uniformly charged. Agreement with the analytic prediction (11) is good when $l > 3\kappa^{-1}$. The computed values tend to 1 as the rod shrinks to a point, whilst the analytic prediction, proportional to l, becomes too small, as discussed in §2. At large l the computed results are slightly smaller than the asymptotic predictions. This reflects the smearing-out of the charge cloud near the ends, which was neglected in the asymptotic analysis. The agreement of these results with the previous analysis of free-draining rods is a useful check on the accuracy of the program, as is the agreement of the friction coefficients with those of Russel *et al.* To explain the experiments, however, we must now study rods with no-slip boundary conditions on their surfaces.

Rods with no-slip boundary conditions

After normalization, the asymptotic result (10) obtained in §3 for a long rod is

$$\mu^*_{\mathrm{NS}} = l\kappa(\log a\kappa)^2/4(\log a/l)^2 \quad (l \gg \kappa^{-1} \gg a). \tag{15}$$

The presence of the rod, rather than a string of free-draining beads, substantially reduces the flow, and thereby reduces the perturbation and the electroviscous effect. This can be seen in figure 6; the curves for the two types of particle are otherwise very similar. In figure 7 we again study the case of three charges placed on rods of various lengths. Again there is an increase in the electroviscous effect as l becomes large. This time, however, there is first a decrease, for as the rod grows longer the flow in the neighbourhood of the central charge is reduced, and this charge eventually gives a negligible contribution to the electroviscous effect. In figure 9 we study uniformly charged rods. The number of charges N is chosen so that the charge spacing is 4,

which is small compared with the cloud size $\kappa^{-1} = 10$. However, from figure 6 we see that a spacing of 10 is quite satisfactory, and this had to be used for the longest rods to keep the computation time short. The analytic prediction (15) is marked by a broken line. We see that the asymptotic result is not valid until $l > 20\kappa^{-1}$. We again ascribe the difference when l is very large to the simplifying assumptions made in §3. The agreement is poorer than in figure 8 (free-draining rods), and occurs only at much larger values of l. This suggests that the major error of §3 was in the velocity field rather than in the assumption of a uniform charge cloud.

Domard's experiments

Domard (1976) performed a series of experiments on suspensions of the peptide poly-α-L-glutamic acid. When ionized the helical structure breaks down, and he concluded that the molecules could then be modelled as rigid cylinders of radius $a = 4 \times 10^{-10}$ m and length $l = 3{\cdot}6 \times 10^{-10}\,\Pi$ m, where Π is the degree of polymerization. He could control the degree of polymerization, and measured the intrinsic viscosity of suspensions for which Π lay between 20 and 560.

Domard expressed his results in terms of a potential ψ_0 derived from titrations. How far this differs from the ζ-potential is not clear for this molecule, but Katchalsky, Shavit & Eisenberg (1954) studied polymethacrylic acid and found that ψ_0 derived from titration was some 15% higher than the ζ-potential measured by electrophoresis. However, we have already shown that results for thick charge clouds are expressed more naturally in terms of the total charge. The experimental results presented here were performed on completely ionized molecules, each of whose monomers carried a single electronic charge e.

In table 1 we see from the low intrinsic viscosity that the longest polymers were in fact coiled: the electrical repulsions between monomers were insufficient to maintain the rod-like shape. Domard also concluded this from his neutron scattering experiments. We are therefore left with results on the four shortest rods. These were performed at ionic strengths between $9{\cdot}8 \times 10^{-4}$ and $7{\cdot}6 \times 10^{-4}$ moles per litre, so that the Debye length κ^{-1} was typically $30a$, whilst $l/2a$ was at most 22·5. The charge cloud was therefore far from uniform. We have already concluded that linearization of the Poisson–Boltzmann equation will not introduce significant errors. Even if we take Π to be 400 we find from (8) that the ratio γ/D is at most 0·2, so rotary Brownian motion is strong and the ion-Péclet number is small. For the longest rods we obtain a Hartmann number $H = 5$ and from our earlier work (I) we conclude that small Hartmann number theory is valid.

From the definition of Domard's intrinsic viscosity (13) we find that the predicted dimensional electroviscous contribution to the intrinsic viscosity is

$$\mu^*_{\mathrm{NS}} e^2 \Pi / 240\pi\epsilon\kappa\omega k T \mu_0 m, \tag{16}$$

where m, the mass of one monomer, approximately equals $129 \times 1{\cdot}66 \times 10^{-27}$ kg, a value derived from the molecular weight. μ^*_{NS} is approximately one for these short rods (and, incidentally, we see from figure 9 that the asymptotic results of §3 will give predictions which are too small by a factor of about seven). Setting $\mu^*_{\mathrm{NS}} = 1$, (16) is proportional to Π and the corresponding straight line is plotted in figure 10. κ varied slightly between the experiments, but by so little that the variation from the straight line is not noticeable. The numerical model was used to study rods with the

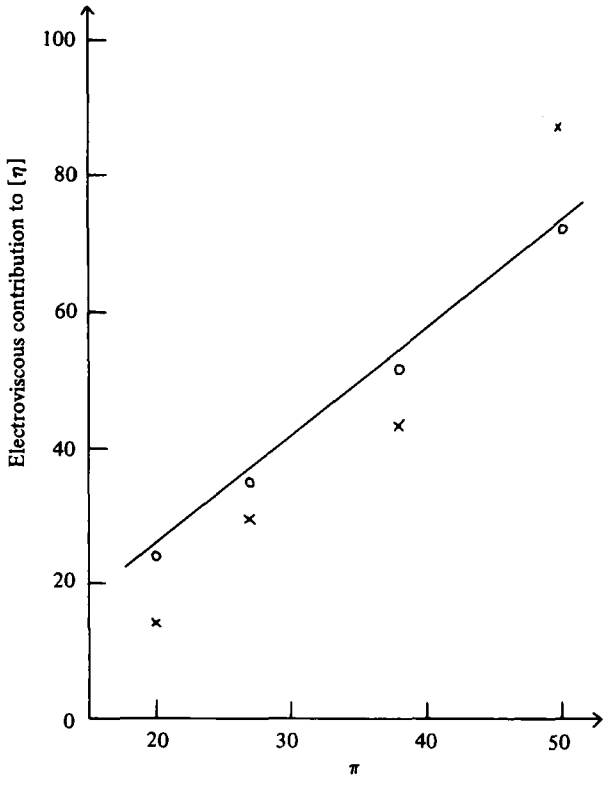

FIGURE 10. Predictions compared with the experimental results. X, experimental results; ——, predictions for point charges ($\mu^* = 1$); ○, the numerical predictions for rod-shaped particles.

	[η]		Electroviscous contribution to [η]		
Π	Experimental	Numerical	Experimental	Theoretical	Experimental / Theoretical
20	26	12	14	24·2	0·58
27	46	17	29	35·3	0·82
38	72	29	43	51·4	0·84
50	130	43	87	70·2	1·2

TABLE 2. Values of the electroviscous contribution to the intrinsic viscosity

same size and charge density as in the experiments, and μ^*_{NS} varied between 0·94 and 0·95. The individual predicted values are shown as isolated points.

The experiments determined only the intrinsic viscosity of a suspension of charged rods. To obtain the electroviscous effect we must subtract the intrinsic viscosity of a suspension of similar, but uncharged, rods. Salt could not be added to compress the double layer and suppress electroviscous effects since that would also have altered the configuration of the molecule. The best we can do is to subtract the theoretical predictions presented in table 1 (assuming $m_T/V = 1$ g cm^{-3}). The resulting experi-

mental results for the electroviscous effect are tabulated in table 2 and plotted on figure 10.

The agreement between theory and experiment is as good as that obtained by Chan & Goring (1966) or by Stone-Masui & Watillon (1968). Here we have the experimental advantage that the electroviscous effect is larger than the intrinsic viscosity of the uncharged molecules. If each monomer is indeed a short cylinder of radius 4×10^{-10} m, length $3{\cdot}6 \times 10^{-10}$ m and mass m, then the obvious computation of V/m_T gives a value 0·845 cm^3 g^{-1}. This reduces the intrinsic viscosity of a suspension of uncharged rods, increases the experimental electroviscous effect, and the ratio of experiment to theory lies between 0·66 and 1·3 (cf. the final column of table 2). Since the agreement is fairly good, small errors such as these can make substantial changes to the percentage error, and there is little point in trying to refine our calculations further. It remains to add that an attempt to obtain the intrinsic viscosity of the long coiled molecules by assuming $\mu^*_{\mathrm{NS}} = 1$ was unsuccessful. A combination of both primary and tertiary electroviscous effects is present in this case.

The bulk of this work was done while the author was a research student in the Department of Applied Mathematics and Theoretical Physics, University of Cambridge. The author is grateful to Professor M. Rinaudo of Grenoble for providing a copy of Domard's thesis and for helpful correspondence, and to his supervisor, Dr E. J. Hinch of Cambridge, for help and encouragement throughout the course of this work, which was supported financially by the Science Research Council.

REFERENCES

Batchelor, G. K. 1970 *J. Fluid Mech.* **44**, 419.
Booth, F. 1950 *Proc. Roy. Soc.* A **203**, 533.
Booth, F. 1954 *J. Chem. Phys.* **22**, 1956.
Chan, F. S. & Goring, D. A. I. 1966 *J. Colloid Interface Sci.* **22**, 371.
Cox, R. G. 1970 *J. Fluid Mech.* **44**, 791.
Domard, A. 1976 Doctoral thesis, University of Grenoble.
Einstein, A. 1911 *Ann. Phys.* **34**, 591.
Higdon, J. J. L. 1979 *J. Fluid Mech.* **90**, 685.
Katchalsky, A., Shavit, N. & Eisenberg, H. 1954 *J. Polymer Sci.* **13**, 69.
Lever, D. A. 1979 *J. Fluid Mech.* **92**, 421.
Lighthill, M. J. 1976 *S.I.A.M. Review* **18**, 161.
Manning, G. S. 1969 *J. Chem. Phys.* **51**, 924.
Riseman, J. & Kirkwood, J. G. 1950 *J. Chem. Phys.* **18**, 512.
Russel, W. B. 1978 *J. Fluid Mech.* **85**, 209.
Russel, W. B., Hinch, E. J., Leal, L. G. & Tieffenbruck, G. 1977 *J. Fluid Mech.* **83**, 273.
Sherwood, J. D. 1980 *J. Fluid Mech.* **101**, 609.
Stone-Masui, J. & Watillon, A. 1968 *J. Colloid Interface Sci.* **28**, 187.
Youngren, G. K. & Acrivos, A. 1975 *J. Fluid Mech.* **69**, 377.